NASA/TM—2008-215204

Reliability Assessment of Graphite Specimens Under Multiaxial Stresses

Steven Sookdeo
Concordia University, Montréal, Québec, Canada

Noel N. Nemeth
Glenn Research Center, Cleveland, Ohio

Robert L. Bratton
Idaho National Laboratory, Idaho Falls, Idaho

August 2008

NASA STI Program . . . in Profile

Since its founding, NASA has been dedicated to the advancement of aeronautics and space science. The NASA Scientific and Technical Information (STI) program plays a key part in helping NASA maintain this important role.

The NASA STI Program operates under the auspices of the Agency Chief Information Officer. It collects, organizes, provides for archiving, and disseminates NASA's STI. The NASA STI program provides access to the NASA Aeronautics and Space Database and its public interface, the NASA Technical Reports Server, thus providing one of the largest collections of aeronautical and space science STI in the world. Results are published in both non-NASA channels and by NASA in the NASA STI Report Series, which includes the following report types:

- TECHNICAL PUBLICATION. Reports of completed research or a major significant phase of research that present the results of NASA programs and include extensive data or theoretical analysis. Includes compilations of significant scientific and technical data and information deemed to be of continuing reference value. NASA counterpart of peer-reviewed formal professional papers but has less stringent limitations on manuscript length and extent of graphic presentations.

- TECHNICAL MEMORANDUM. Scientific and technical findings that are preliminary or of specialized interest, e.g., quick release reports, working papers, and bibliographies that contain minimal annotation. Does not contain extensive analysis.

- CONTRACTOR REPORT. Scientific and technical findings by NASA-sponsored contractors and grantees.

- CONFERENCE PUBLICATION. Collected papers from scientific and technical conferences, symposia, seminars, or other meetings sponsored or cosponsored by NASA.

- SPECIAL PUBLICATION. Scientific, technical, or historical information from NASA programs, projects, and missions, often concerned with subjects having substantial public interest.

- TECHNICAL TRANSLATION. English-language translations of foreign scientific and technical material pertinent to NASA's mission.

Specialized services also include creating custom thesauri, building customized databases, organizing and publishing research results.

For more information about the NASA STI program, see the following:

- Access the NASA STI program home page at *http://www.sti.nasa.gov*

- E-mail your question via the Internet to *help@sti.nasa.gov*

- Fax your question to the NASA STI Help Desk at 301–621–0134

- Telephone the NASA STI Help Desk at 301–621–0390

- Write to:
  NASA Center for AeroSpace Information (CASI)
  7115 Standard Drive
  Hanover, MD 21076–1320

NASA/TM—2008-215204

Reliability Assessment of Graphite Specimens Under Multiaxial Stresses

Steven Sookdeo
Concordia University, Montréal, Québec, Canada

Noel N. Nemeth
Glenn Research Center, Cleveland, Ohio

Robert L. Bratton
Idaho National Laboratory, Idaho Falls, Idaho

National Aeronautics and
Space Administration

Glenn Research Center
Cleveland, Ohio 44135

August 2008

Acknowledgments

This work was funded under Space Act Agreement SAA3–824 with Battelle Energy Alliance and Concordia Institute of Aerospace Design and Innovation.

This work was sponsored by the Fundamental Aeronautics Program at the NASA Glenn Research Center.

Level of Review: This material has been technically reviewed by technical management.

Available from

NASA Center for Aerospace Information
7115 Standard Drive
Hanover, MD 21076–1320

National Technical Information Service
5285 Port Royal Road
Springfield, VA 22161

Available electronically at http://gltrs.grc.nasa.gov

Contents

Reliability Assessment of Graphite Specimens Under Multiaxial Stresses

Steven Sookdeo
Concordia University
Montréal, Québec, Canada H3G 1M8

Noel N. Nemeth
National Aeronautics and Space Administration
Glenn Research Center
Cleveland, Ohio 44135

Robert L. Bratton
Idaho National Laboratory
Idaho Falls, Idaho 83415

Summary

An investigation was conducted to predict the failure strength response of IG−100 nuclear grade graphite exposed to multiaxial stresses. As part of this effort, a review of failure criteria accounting for the stochastic strength response is provided. The experimental work was performed in the early 1990s at the Oak Ridge National Laboratory (ORNL) on hollow graphite tubes under the action of axial tensile loading and internal pressurization. As part of the investigation, finite-element analysis (FEA) was performed and compared with results of FEA from the original ORNL report. The new analysis generally compared well with the original analysis, although some discrepancies in the location of peak stresses were noted. The Ceramics Analysis and Reliability Evaluation of Structures Life prediction code (CARES/Life) was used with the FEA results to predict the quadrant I (tensile-tensile) and quadrant IV (compression-tension) strength response of the graphite tubes for the principle of independent action (PIA), the Weibull normal stress averaging (NSA), and the Batdorf multiaxial failure theories. The CARES/Life reliability analysis showed that all three failure theories gave similar results in quadrant I but that in quadrant IV, the PIA and Weibull normal stress-averaging theories were not conservative, whereas the Batdorf theory was able to correlate well with experimental results. The conclusion of the study was that the Batdorf theory should generally be used to predict the reliability response of graphite and brittle materials in multiaxial loading situations.

1. Introduction

1.1 Graphite and Next-Generation Nuclear Reactors

There is a renewed interest in nuclear energy because nuclear power plants generate zero greenhouse gas emissions, and new reactor technologies may enable hydrogen cogeneration (for the hydrogen economy). At present, 10 countries, including the United States, have agreed to cooperate in the development of the fourth-generation (Gen IV) nuclear energy system to help meet the world's growing energy needs (Generation IV International Forum (2007)). Figure 1 shows the evolution of reactors since their introduction in the 1950s.

The expectation is that these Gen IV reactors will be gas cooled and will run at high temperatures (up to 950 °C) using graphite (instead of water) as the moderator material (see fig. 2). The ultimate goal of the initiative is to develop a system that is sustainable, economical, safe, reliable, and resistant to proliferation (MacDonald (2005), Generation IV International Forum, and the U.S. DOE Nuclear Energy Research Advisory Committee (2002)). The Gen IV system is expected to come into service in 2030. NASA has

complimentary interest in this endeavor with regard to the development of lunar/Mars surface power generation and nuclear propulsion for interplanetary missions.

In the United States, Gen IV research is being conducted by the U.S Department of Energy (DOE) for development of the very high-temperature reactor (VHTR) design concept for the next-generation nuclear plant (NGNP) project (MacDonald (2005)). The reactor design will be a graphite-moderated reactor, either a prismatic graphite block-type core or pebble bed core that will produce electricity and hydrogen in a highly efficient manner. The NGNP will have a projected service life of 60 years and will be designed to ensure passive decay heat removal without fuel damage or radioactive material releases

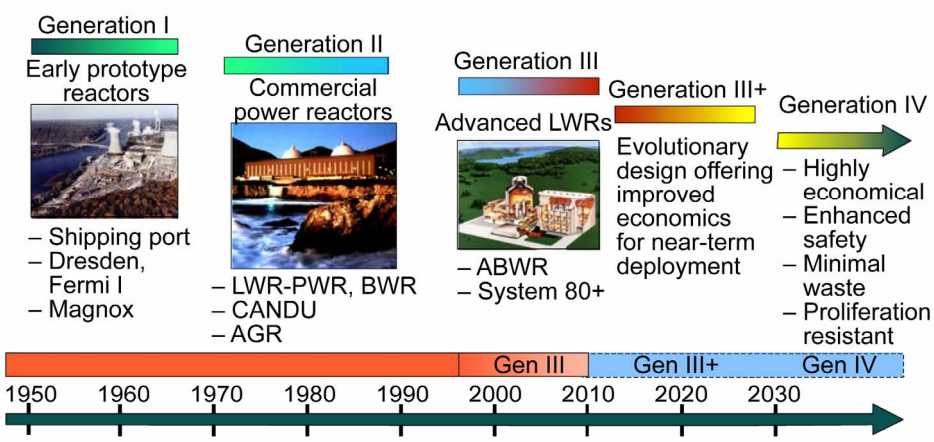

Figure 1.—Developmental timeline of generations I to IV. Light water reactor (LWR); pressurized heavy water reactor (PWR); boiling water reactor (BWR); Canada deuterium uranium reactor (CANDU); advanced gas-cooled reactor (AGR); advanced boiling water reactor (ABWR). Reproduced from Generation IV International Forum and the U.S. DOE Nuclear Energy Research Advisory Committee (2002).

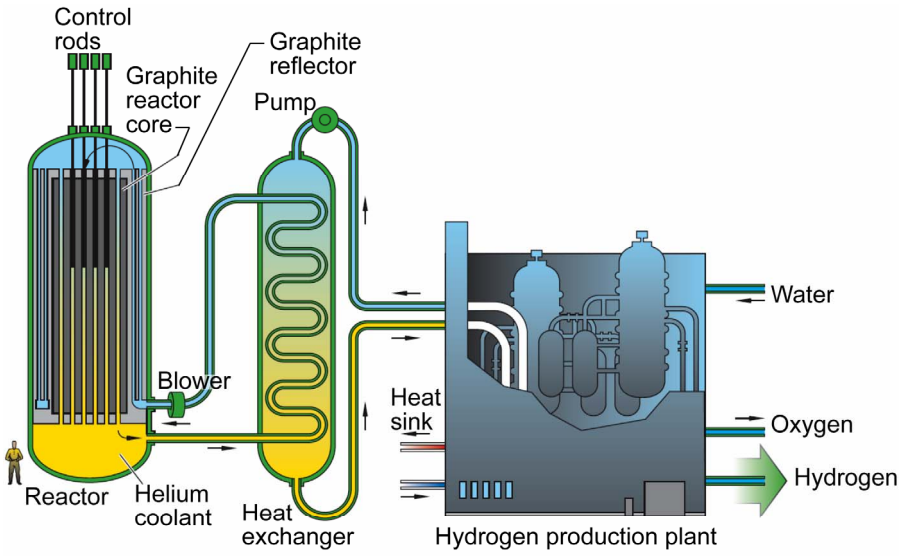

Figure 2.—Gen IV gas-cooled, very high-temperature reactor (VHTR) using graphite for neutron reflection and moderation within reactor core. Reproduced from Generation IV International Forum and the U.S. DOE Nuclear Energy Research Advisory Committee (2002).

during accidents. Important to the NGNP project are design methods development and validation for the graphite structures used in the reactor. The reason for this importance is that large amounts of graphite (up to thousands of tons) would be required for the core of the reactor, and significant loads may be experienced by the individual graphite bricks that surround the nuclear fuel. An example of in-core graphite components is shown in figure 3 for an earlier generation II reactor design. Of particular concern is the potential for crack formation and even rupture in individual blocks. Therefore, failure theories and/or effective design strategies that predict and can mitigate failure from fracture are desired.

The purpose of this report is to examine how well the multiaxial strength response of a particular grade of graphite can be predicted using available fracture models developed for brittle materials. Graphite may not act in a truly brittle manner; hence, it would be of interest to test to determine if these models were still relevant. The principle of independent action (PIA), Weibull normal stress-averaging (NSA), and Batdorf theories were used to predict the multiaxial strength response, which is an important step in the development of an accepted design methodology for graphite structures. The experimental data from this project come from previous data available in the literature. Finite-element analysis (FEA) was used to model the graphite specimens, and results were extensively compared with analysis previously performed and reported in the literature. The validated finite-element model may be useful for future high-temperature testing. Also, regions of stress concentration that were identified as potential areas of concern should warrant further scrutiny. The NASA-developed CARES/Life (Ceramics Analysis and Reliability Evaluation of Structures Life prediction) code (Nemeth, et al. (1993, 2003, 2005)) along with the results from the FEA were then used for the aforementioned theories to predict the stochastic strength response of the graphite specimens under multiaxial stresses. Only the behavior of unirradiated graphite is examined herein.

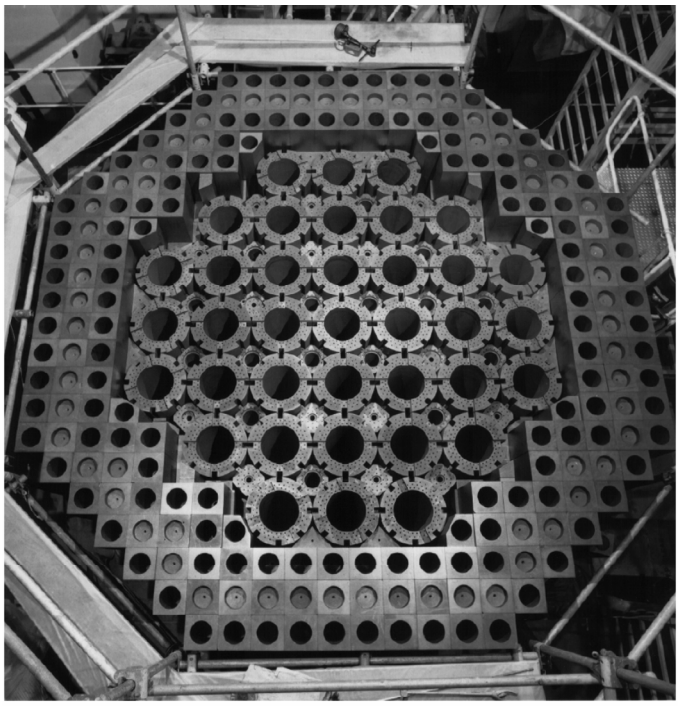

Figure 3.—Graphite components in United Kingdom advanced gas-cooled reactor (AGR) before fuel insertion. Individual components assembled with block-and-key construction (Holt, http://www.eng.hull.ac.uk/research/Graphite/index.htm).

1.2 Modeling Brittle Materials

Graphite behavior ranges from brittle to quasi-brittle, and the strength of graphite is stochastic. Traditional material failure analyses employing a deterministic approach, where failure is assumed to occur when some allowable stress level or equivalent stress is exceeded, are not adequate for brittle material component design. Such phenomenological failure theories are reasonably successful when applied to ductile materials such as metals. However, since analysis of failure in components fabricated from brittle materials is governed by the observed scatter in strength, statistical design approaches must be used to accurately reflect the stochastic physical phenomena that determine material fracture response. Accounting for these phenomena requires a change in philosophy on the design engineer's part, leading to a reduced focus on the use of safety factors in favor of reliability analyses. If a brittle material with an obvious scatter in tensile strength is selected, then components should be designed using an appropriate design methodology rooted in statistical analysis. However, the reliability approach demands that the design engineer tolerate a finite risk of unacceptable performance. This risk of unacceptable performance is identified as a component's probability of failure (or alternatively, component reliability). The primary concern of the engineer is minimizing this risk in an economical manner.

Brittle materials lack ductility and yielding capability, which leads to low strain tolerance, low fracture toughness, and large variations in observed fracture strength. When a load is applied, the absence of significant plastic deformation causes large stress concentrations to occur at microscopic flaws, which are unavoidably present as a result of materials processing operations. The observed scatter in component strength is caused by the variable severity of these flaws and by the behavior of sudden catastrophic crack growth, which occurs when the crack driving force or energy release rate reaches a critical value. Therefore, an appropriate probabilistic design methodology combines the statistical nature of strength-controlling flaws with the mechanics of crack growth to allow for multiaxial stress states, concurrent (simultaneously occurring) flaw populations, and component size and/or scaling effects. These are accounted for in the CARES/Life program.

1.3 CARES/Life Design Software Overview

The CARES/Life software describes the probabilistic nature of material strength using the Weibull cumulative distribution function (Weibull (1951)). The effect of multiaxial stresses on reliability is predicted by using the PIA (Barnett, et al. (1967) and Freudenthal (1968)), the Weibull NSA method (Weibull (1939)), or the Batdorf theory (Batdorf and Crose (1974) and Batdorf and Heinisch (1978)). The methodologies for predicting component reliability and estimating Weibull parameters are explained in Nemeth, et al. (2003) and (2005). The following is a brief summary.

Input for CARES/Life includes material data from simple experiments and results from a FEA of a complex component. The simple fracture experiments are typically tensile or flexural strength tests performed on many (recommended to be 30 or more) nominally identical specimens. From the failure data, statistical strength parameters (Weibull distribution parameters) are estimated using maximum likelihood or least-squares regression. Finite-element heat-transfer and linear-elastic stress analyses are used to determine the component temperature and stress distributions. The reliability at each element (actually at each Gaussian integration point of an element) is calculated from the respective stress distribution and the associated volume or area in conjunction with the Weibull parameters associated with that element's particular temperature (normalized to a unit volume or area). The overall component reliability is the product of all the element survival probabilities. The component reliability is computed assuming that randomly distributed volume flaws and/or surface flaws control the failure response.

CARES/Life uses the two-parameter Weibull distribution. For a uniaxially stressed component, the two-parameter Weibull distribution is expressed as

$$P_{fV} = 1 - \exp\left[-\frac{1}{{\sigma_{oV}}^{m_V}} \int_V \sigma(x,y,z)^{m_V}\, dV \right] \tag{1}$$

where P_{fV} is the probability of failure; V is the volume; V as a subscript denotes a volume-dependent property; $\sigma(x,y,z)$ is the uniaxial stress at a point location in the body; m_V is the volume-dependent shape parameter; and σ_{oV} is the volume-dependent scale parameter of the Weibull distribution. The shape parameter is a measure of the dispersion of strength whereas the scale parameter is the strength of a unit volume of material at 63.21 percent probability of failure. An analogous equation based on area can be shown for flaws residing on the surface of the component. The Weibull equation is based on the weakest link theory, which assumes that the structure is analogous to a chain with many links and that each link may have a different limiting strength. When a load is applied to the structure such that the weakest link fails, then the structure fails.

For CARES/Life, the effect of multiaxial stresses on reliability is predicted by using either PIA, the Weibull NSA, or the Batdorf theory. For the PIA model, the reliability of a component under multiaxial stresses is the product of the reliability of the individual principal stresses, $\sigma_1, \geq\sigma_2, \geq\sigma_3$, acting independently. For volume-distributed flaws this is

$$P_{fV} = 1 - \exp\left[-k_{wV} \int_V \left(\sigma_1^{m_V} + \sigma_2^{m_V} + \sigma_3^{m_V} \right) \mathrm{d}V \right] \tag{2}$$

where $k_{wV} = (\sigma_{oV})^{-m_v}$ is the Weibull crack-density coefficient. The NSA method involves the integration and averaging of tensile normal stress components evaluated about all possible orientations and locations. This approach is a special case of the more general Batdorf theory and assumes the material to be shear insensitive. The NSA equation is described by

$$P_{fV} = 1 - \exp\left(-\int_V k_{wpV}\, {\overline{\sigma}_n}^{m_V}\, \mathrm{d}V \right) \tag{3}$$

where

$${\overline{\sigma}_n}^{m_V} = \frac{\int_A \sigma_n^{m_V}\, \mathrm{d}A}{\int_A \mathrm{d}A} \tag{4}$$

The area integration is performed in principal stress space over the surface A of a sphere of unit radius for regions where σ_n, the projected normal stress on the surface, is tensile. The polyaxial Weibull crack-density coefficient k_{wpV} is

$$k_{wpV} = \left(2m_V + 1\right) k_{wV} \tag{5}$$

The Batdorf theory combines the weakest link theory and linear elastic fracture mechanics (LEFM). Conventional fracture mechanics analysis requires that both the size of the critical crack and its orientation relative to the applied loads determine the fracture stress. The Batdorf theory includes the calculation of the combined probability of the critical flaw being within a certain size range and being located and oriented so that it may cause fracture. The probability of failure for a ceramic component using the Batdorf model for volume flaws can be expressed as

$$P_{fV} = 1 - \exp\left[-\frac{2}{\pi} \int_V \int_0^{\pi/2} \int_0^{\pi/2} \eta_V\left(\sigma_{Ieq}\right) \sin\alpha\, \mathrm{d}\alpha\, \mathrm{d}\beta\, \mathrm{d}V \right] \tag{6}$$

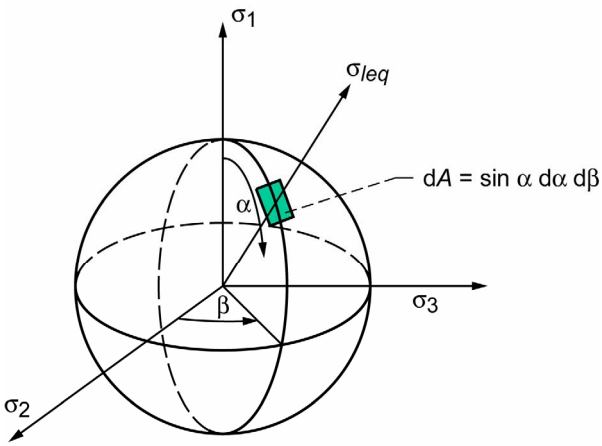

Figure 4.—Unit radius sphere representing all possible flaw orientations.

For a sphere of unit radius, an elemental surface area of the sphere is dA = sin α dβ dα where α and β are orientation angles as shown in figure 4. The unit radius sphere is used to determine the probability of a flaw being oriented such that it may cause fracture.

An infinitesimal area dA on the unit sphere represents a particular flaw orientation (a direction normal to the flaw plane), and σ_{Ieq} is an equivalent stress which is a function of an assumed crack shape and multiaxial fracture criterion.

In this case because of symmetry of stresses, this integration is only performed over one-eighth of the sphere. The crack-density function is

$$\eta_V\left(\sigma_{Ieq}\right) = k_{BV}\,\sigma_{Ieq}^{m_V}\left(x, y, z, \alpha, \beta\right) \tag{7}$$

where η_V represents the number of flaws per unit volume having a strength equal to or less than σ_{Ieq}, and the Batdorf crack-density coefficient k_{BV} is a function of k_{wV} and the mixed-mode fracture criterion chosen. It is described further in the CARES/Life papers previously mentioned.

The effective stress σ_{Ieq} represents an equivalent normal stress on the crack face from the combined action of the normal stress σ_n and the shear stress τ on the crack face, oriented normal to α and β. For a penny-shaped crack with the Shetty mixed-mode fracture criterion, the effective stress becomes

$$\sigma_{Ieq} = \frac{1}{2}\left\{\sigma_n + \sqrt{\sigma_n^2 + \left[\frac{4\tau}{\overline{C}\left(2-\nu\right)}\right]^2}\right\} \tag{8}$$

where ν is Poisson's ratio and $\overline{C}$ is the Shetty shear-sensitivity coefficient, with values typically in the range $0.80 \le \overline{C} \le 2.0$. As $\overline{C}$ increases, the response becomes progressively more shear insensitive. For a penny-shaped crack with a material having a Poisson's ratio of about 0.22 and $\overline{C}$ = 0.80, 0.85, 1.05, and 1.10, equation (8) models, respectively, the following criteria: Ichikawa's maximum energy release rate approximation, the maximum tangential stress, Hellen and Blackburn's maximum strain-energy release rate formulation, and colinear crack extension. The value of $\overline{C}$ can also be used to empirically fit to experimental data, which is done in this study. As previously mentioned, further details can be found in the CARES/Life papers.

To calculate a component's failure probability, results from FEA are used. FEA enables the discretization of the component into incremental volume elements. For enhanced numerical accuracy, the stress state and volume associated with an element's Gaussian integration points are used. Using the information associated with the element integration points subdivides the element into subelements, where V_{isub} corresponds to the volume of an individual subelement. The stress state, temperature, and environment for each subelement are assumed to be uniform throughout its volume. In this case, the volume integrals described in the previous equations are replaced with a volume summation. There are many other parameters that can be adjusted to generate results for a specific problem. As an example, for problems that involve multiple time steps, CARES/Life can solve for the reliability of a specific time step or a range of time steps.

The appendix presents a comparison of stresses along the inner surface versus the results from the ORNL reports (Hobson, D.O. (1994) and Yahr, et al. (1993) (Multiaxial Tests of H–451 Graphite. ORNL/NPR–93/13, vol. 1, not published. Available from Carbon Materials Technology Group, ORNL.)) in English units.

2. Multiaxial Testing and Reliability Analysis of Graphite

2.1 Graphite Specimen Description

Researchers at ORNL have developed and reported on a specimen geometry and test facility used to test H–451- and IG–110-grade graphite under a combination of internal pressure and axial load (Rittenhouse (1995), Eto, et al. (1996), Hobson, D.O. (1994), and Yahr, et al. (1993) (Multiaxial Tests of H–451 Graphite. ORNL/NPR–93/13, vol. 1, not published. Available from Carbon Materials Technology Group, ORNL.)). The specimens were put under axial tension using a grip system, and an expanding bladder inside the tube was used to apply the internal pressure. Figure 5 shows a schematic of the loading fixture and figure 6 shows a graphite multiaxial specimen. The specimen was designed such that within its gauge section (the center section of constant cross-sectional area), the stresses should be uniform. To verify the results of the testing and help to refine the specimen design, the ORNL researchers constructed a finite-element model using PATRAN (MSC Software Corporation) and the ADINA FEA code (ADINA R & D, Inc.) and also compared predicted stresses with strain gauge results.

2.2 Modeling Approach

A finite-element model was created in ANSYS version 9.0 (ANSYS Inc.) using information in the ORNL report. The results from this analysis are compared with the results in the ORNL report, which was analyzed with ADINA, to validate the new finite-element model. Note that CARES/Life does not accept results from ADINA. Also, the new ANSYS model that was prepared had a significantly higher mesh density than the ORNL model. CARES/Life is sensitive to stress gradient (since in CARES/Life stress is raised by the exponent of the Weibull modulus (e.g., see eq. (7)), and a refined mesh is required for an accurate (converged) probability of failure prediction. With an acceptable model, the CARES/Life program could be confidently used to predict the multiaxial strength response.

As in the ORNL report, the benchmarking of the FEA was done with an axial load applied, with an internal pressure applied, and with both loads applied together. The results were graphed and compared with calculated values.

In this report only the IG–110-grade graphite is modeled. The material properties can be found at Toyo Tanso Co., LTD. (2006). The IG–110 is a near-isotropic grade of graphite. The HT–451-grade graphite described in Rittenhouse (1995), Eto, et al. (1996), Hobson, D.O. (1994), and Yahr, et al. (1993) (Multiaxial Tests of H–451 Graphite. ORNL/NPR–93/13, vol. 1, not published. Available from Carbon Materials Technology Group, ORNL.) showed significant strength anisotropy. The CARES/Life program only models isotropic brittle materials. Hence, HT–451 is not modeled herein, and IG–110 is assumed to have isotropic strength and material properties in the subsequent analysis. Note that stress analysis results

reported herein are for IG–110 material properties but that ORNL reported stress results were consistent for HT–451 material.

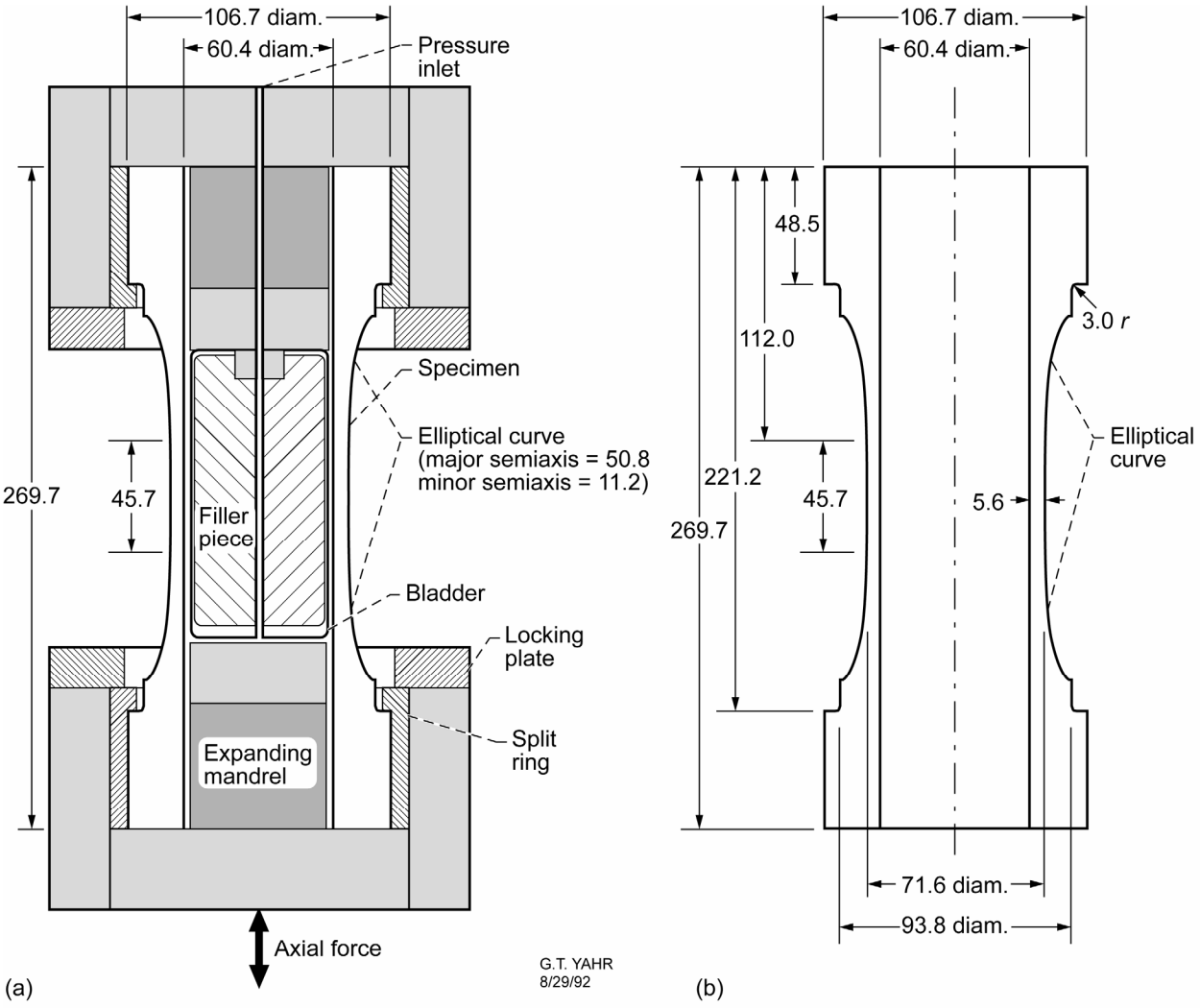

Figure 5.—Oak Ridge National Laboratory multiaxial specimen. (a) Cross section of specimen and grip system. (b) Cross section of specimen. (Dimensions are in millimeters.)

Figure 6.—Oak Ridge National Laboratory multiaxial specimen with strain gauges.

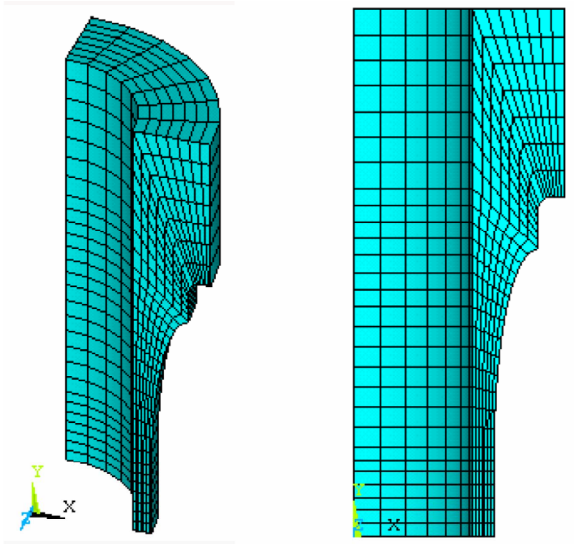

(a) (b)

Figure 7.—ANSYS model of graphite tube specimen. A 90° segment of top half of specimen is modeled. (a) Isometric view. (b) Front view.

2.3 ANSYS Finite-Element Model

The finite-element model was created using ANSYS 9.0. Due to symmetry, the top half of a 90° section was modeled with appropriate constraints applied. It was meshed so that there were five quadrilateral divisions through the cross section, enabling the use of Solid 95 isoparametric brick elements (fig. 7). Because of symmetry, nodes in the x,z-plane were constrained in the y-direction at the midplane of the specimen (bottom face of fig. 7), and appropriate x- and z-direction constraints were applied to the appropriate faces of the model cross section. Axial load was applied where the split ring gripped the specimen, and internal pressurization was applied where the bladder contacted the inner diameter surface of the specimen as shown in figure 5. All loads were applied using metric units. For this analysis, the material model used was an isotropic linear elastic type. Young's modulus E = 10.5 GPa and Poisson's ratio ν = 0.15 were used, which differ somewhat from what are listed at Toyo Tanso Co., LTD. (2006) but correspond to the values used by ORNL. However, if the effect of the displacement of the mandrel is ignored and if it is assumed that all deformations are small, then the stress solution is essentially independent of the value of elastic constants typically used for graphite. The reason is that loading was done by applying force (pressure), and the enforced boundary conditions did not constrain the growth of the specimen. Therefore, stress solution results that use different elastic constants (say for the HT–110 material) are very comparable for high-elastic-modulus (high stiffness) materials.

3. Modeling and Results

3.1 Application of Loads

3.1.1 Application of axial load

Axial tensile force was applied as a pressure on the area that represents the grip (the lip of the split ring shown in fig. 5(a)). For example, for a 17.8-kN (4000-lb) force, the pressure applied on the grip bearing area was

$$\text{Area} = \pi\left(r_o^2 - r_i^2\right) = \pi\left[(53.35)^2 - (48.49)^2\right] = 1615.34\ \text{mm}^2$$

$$\text{Pressure} = \frac{F}{A} = \frac{17\,800\ \text{N}}{1615.34\ \text{mm}^2} = 11.01\ \text{MPa} \tag{9}$$

where r_o is the radial distance to the outer edge of the specimen (the outer radius of the lip of the split ring), and r_i is the radial distance to the second farthest outer edge (the inner radius of the lip of the split ring) of the specimen.

This loading was used to help validate the ANSYS model versus results provided in the ORNL reports. Compressive stresses were obtained by applying pressure to the top (and bottom) face of the specimen.

3.1.2 Application of internal pressure

Pressure was applied on the area covering the middle 117.348 mm (4.62 in.) of the inside surface corresponding to the location of the internal bladder as shown in figure 5(a). An internal pressure of 2.84 MPa (412 psi) was used to help validate our model versus results provided in the ORNL reports.

3.1.3 Radial displacement

In the ORNL reports (Rittenhouse (1995), Eto, et al. (1996), Hobson, D.O. (1994), and Yahr, et al. (1993) (Multiaxial Tests of H–451 Graphite. ORNL/NPR–93/13, vol. 1, not published. Available from Carbon Materials Technology Group, ORNL.)), a fixed displacement of 0.0381 mm (0.0015 in.) was applied on the model. It represented an expanding mandrel that was placed inside the graphite tube to a depth of 48.5 mm (1.909 in.) during the experiments. The purpose of the mandrel was to minimize the amount of fluid in the specimen (when applying the internal pressure). This displacement was not included in the ANSYS model used in the CARES/Life reliability analysis. Its effects were shown to be negligible in the gauge section of the specimen where stresses were highest.

3.1.4 Validation cases tested

A stress analysis was run for three cases to validate the model in comparison with the ORNL analysis: the first was to determine the effects of the axial force; the second, to determine the effects of the internal pressure; and the third, to determine the combined effect of the force and pressure. As in the ORNL report, the inner and outer surfaces (gauge length) of the specimen were analyzed. Using the ANSYS model, the stress distribution through the specimen wall at the center of the gauge section was also produced (through the specimen wall at the bottom of fig. 7(b)). This is also denoted in this report as the center section—the horizontal plane of symmetry, through the thickness.

3.2 Effect of Axial Force

3.2.1 ANSYS finite-element results: axial force

The ANSYS finite-element model was solved with an 11.01-MPa (1597-psi) pressure applied on the areas that represent the grips; it simulated the 17.8-kN (4000-lb) load.

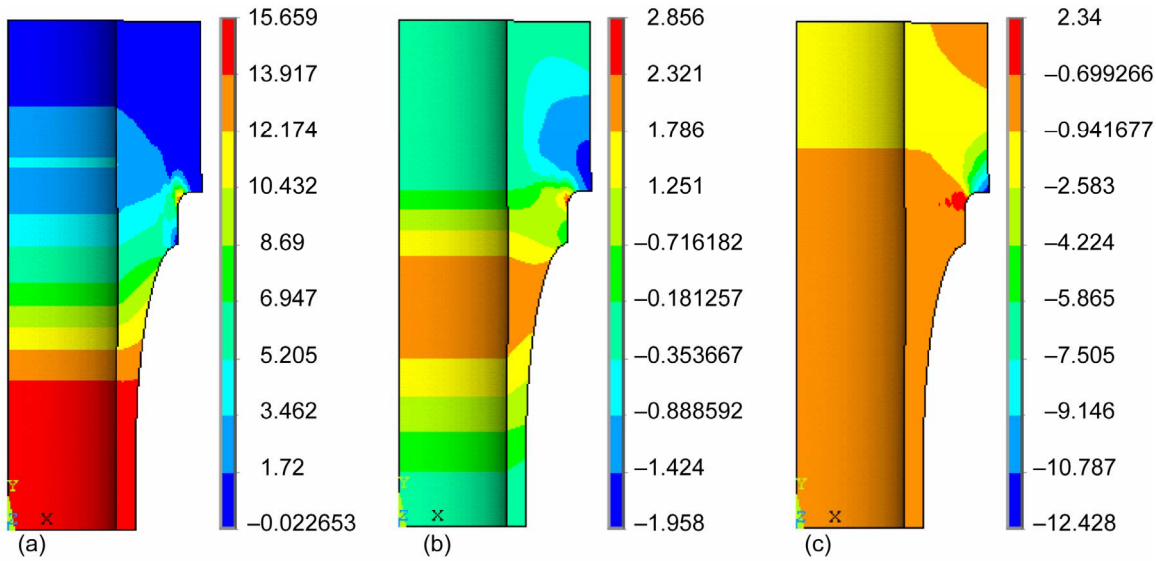

Figure 8.—Effect of 17.8 kN [4000-lb] axial force. (a) First principal stress. (b) Second principal stress. (c) Third principal stress.

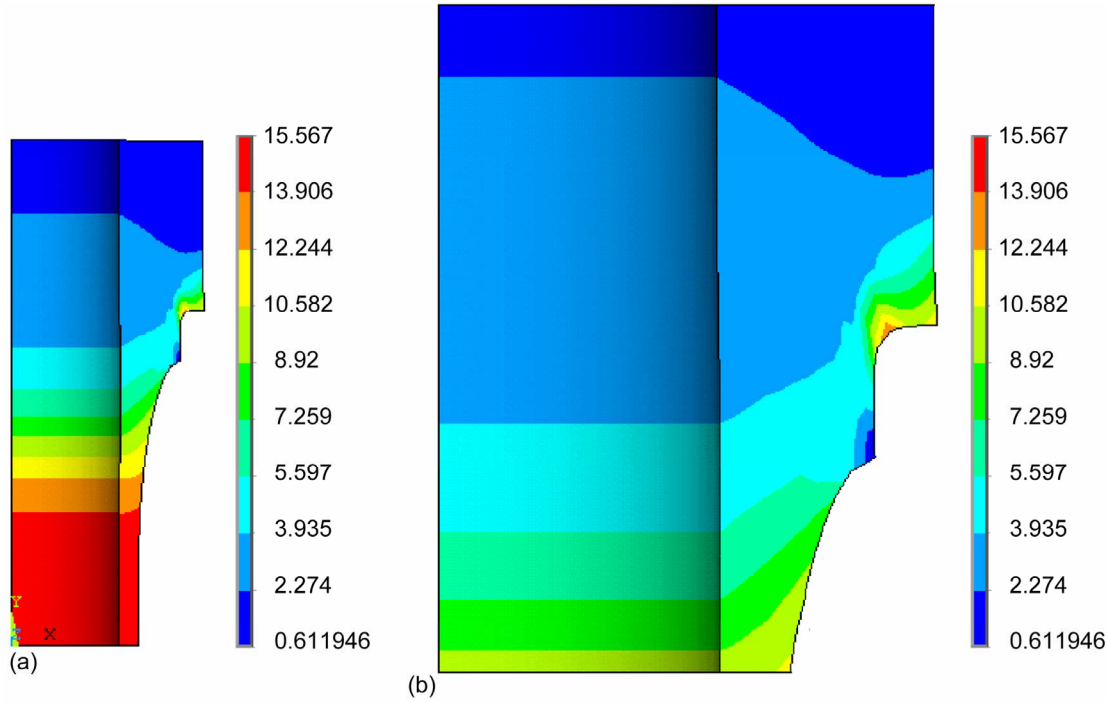

Figure 9.—Von Mises stress distribution from applied axial force. (a) Von Mises stress. (b) Closeup of transition and grip regions plotting Von Mises stress.

The finite-element model had the stress distributions shown in figure 8. In the transition region, there was no large stress gradient shown. It can be inferred that there are no significant stress concentrations in this region. However, figure 8(a) for Von Mises stress shows a stress concentration at the fillet adjacent to where the axial force was applied. A closeup of this region shown in figure 9(b) shows that the maximum stress of 13.91 MPa (2017 psi) at the fillet is less than the stress of 15.57 MPa (2258 psi) in the gauge section. The plot of Von Mises stress is used in this case for illustration purposes and is essentially a representative effective stress. That the Von Mises stress at the fillet was less than the maximum stress in

the gauge section means that specimen fracture was more likely to occur in the gauge section as intended rather than in the fillet region. But the relatively high stress at the fillet is undesirable, and an alteration of the specimen design in the future would be prudent if feasible.

3.2.2 Effect of axial force: inner surface

On the inner surface, the peak axial stress was 15.66 MPa (2271 psi) at a location 15.91 mm (0.63 in.) from the center (midpoint) of the gauge section. The axial stress at the center of the specimen was 15.49 MPa (2247 psi). This value compares with a calculated value of 15.33 MPa (2223 psi) simply determined by taking the applied force divided by the cross-sectional area. The ORNL report presented the calculated axial stress at the center to be 15.59 MPa (2261 psi). The difference between ORNL and NASA may be due the improved mesh density of the ANSYS model and slight differences in applied load. The difference from the calculated value is due to the specimen geometry where the axial stress through the wall thickness is not completely uniform. The axial stress stayed relatively constant along the gauge section length, as it should.

These results are comparable to the results that were presented in the ORNL report. Table I shows that the difference in stress between the ANSYS results and the numerical results is less than 1 percent. The axial location of the peak stress is not at the center of the gauge section, but rather is somewhat offset. The offset is caused by the effects of specimen geometry. The difference between the NASA results and the ORNL results is likely attributed to slight differences in loading: the NASA model ignored the enforced displacement of the mandrel (to reduce the amount of iterations required to obtain the CARES/Life answers for a given level of failure probability) and the ORNL did not. Also, the NASA mesh was considerably more refined than the ORNL mesh. Last, the stress magnitude was relatively constant across the gauge length so that the location of peak stress was not too significant an issue (see the appendix).

TABLE I.—COMPARISON OF NUMERICAL RESULTS: EFFECT OF AXIAL FORCE ON INNER SURFACE

Finite-element analysis	Axial stress at center, MPa (psi)	Peak axial stress, MPa (psi)	Axial location[a] of peak stress, mm (in.)
ORNL	15.59 (2261)	15.66 (2271)	10.16 (0.40)
NASA	15.49 (2247)	15.66 (2271)	15.91 (0.63)
Difference, percent	0.6	0.0	[b]26

[a]Measured from center of specimen.
[b]Percentage difference relative to one-half gage length.

The stress at the center of the gauge section was slightly higher than that calculated from a simple force/area calculation as shown in table II.

TABLE II.—COMPARISON OF CALCULATED RESULTS: EFFECT OF AXIAL FORCE

Results	Axial stress at center, MPa (psi)
Calculated	15.33 (2223)
NASA (finite-element analysis)	15.49 (2247)
Difference, percent	1.0

Figure 10 is a plot of the stresses on the inner surface versus axial distance from the specimen center. The appendix presents a comparison of stresses along the inner surface versus the results from the ORNL reports (Hobson, D.O. (1994) and Yahr, et al. (1993) (Multiaxial Tests of H–451 Graphite. ORNL/NPR–93/13, vol. 1, not published. Available from Carbon Materials Technology Group, ORNL.)) in English units. It can be seen that the stress results are comparable but have slight differences, which are deemed negligible for the CARES/Life reliability analysis. Note that comparable stress profile results for the outer surface are not available.

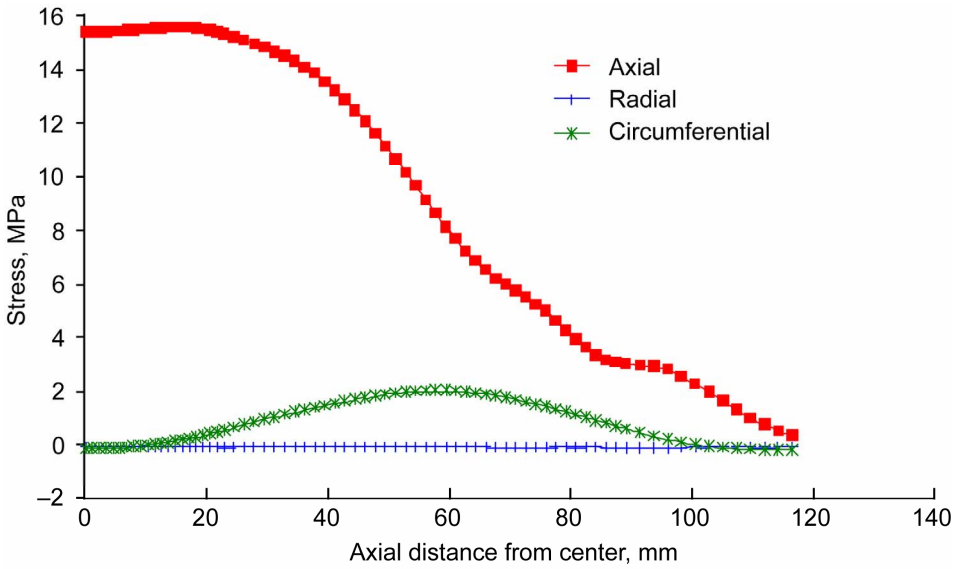

Figure 10.—Effect of axial force. Stress distribution on inner surface (axial distance from centerline).

In general, the ANSYS results follow the trends produced in the ORNL report. The axial stress peaks later in the ANSYS model at approximately 15 mm (0.59 in.) instead of at 10 mm (0.39 in.). Also, the circumferential stress deviated slightly from the ORNL report after 100 mm (3.94 in.), which became slightly compressive most likely because the ANSYS model did not apply the radial displacement of the mandrel. This did not affect the accuracy of the CARES/Life reliability analysis since the failure probability predictions are dominated by the high stresses in the gauge section.

3.2.3 Effect of axial force: outer surface

The axial stress on the outer surface of the gauge section peaked at 15.31 MPa (2221 psi) at the end of the gauge section just prior to the transition region. Again, the axial stress stayed relatively constant within the gauge section, as it should.

The results from the ANSYS model agree within 1 percent with the original finite-element results in the ORNL report (see table III).

TABLE III.—COMPARISON OF NUMERICAL RESULTS: EFFECT OF AXIAL FORCE

Finite-element analysis	Axial stress at center, MPa (psi)
ORNL NASA	15.02 (2178) 15.16 (2199)
Difference, percent	0.9

A plot of the stresses along the gauge section from the FEA is shown in figure 11.

The general trend in the gauge section from the ORNL report was mimicked by the ANSYS results. There was an increase in the axial stress to a maximum near 22 mm (0.86 in.) near the transition region. Additionally, the circumferential stress increased ahead of the radial stress. This indicated a slight stress concentration at the beginning of the transition region. Any level of stress concentration is undesirable, but in this case it is probably tolerable (meaning a disproportionally high percentage of failures would not occur at this location).

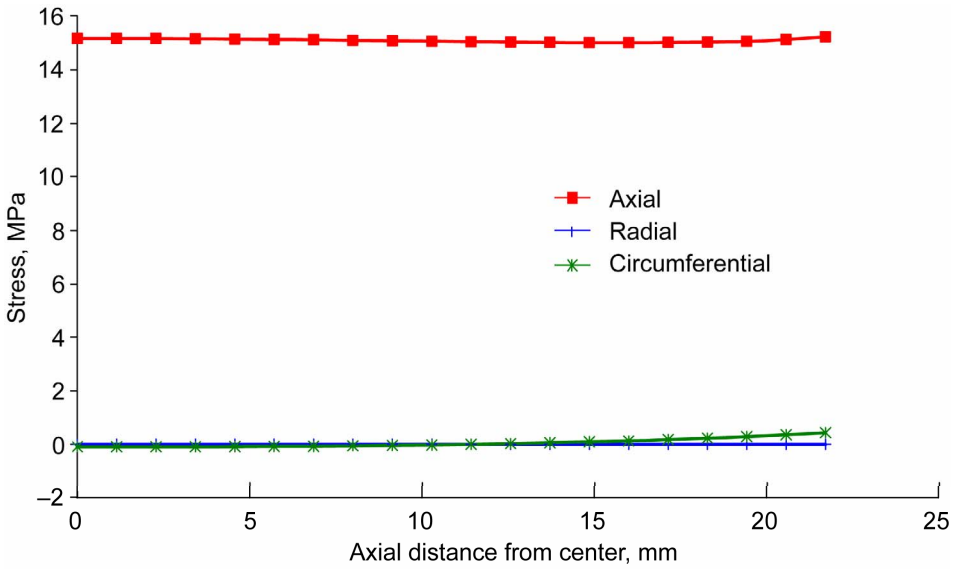

Figure 11.—Effect of axial force. Stress distribution on outer surface within gage section of specimen.

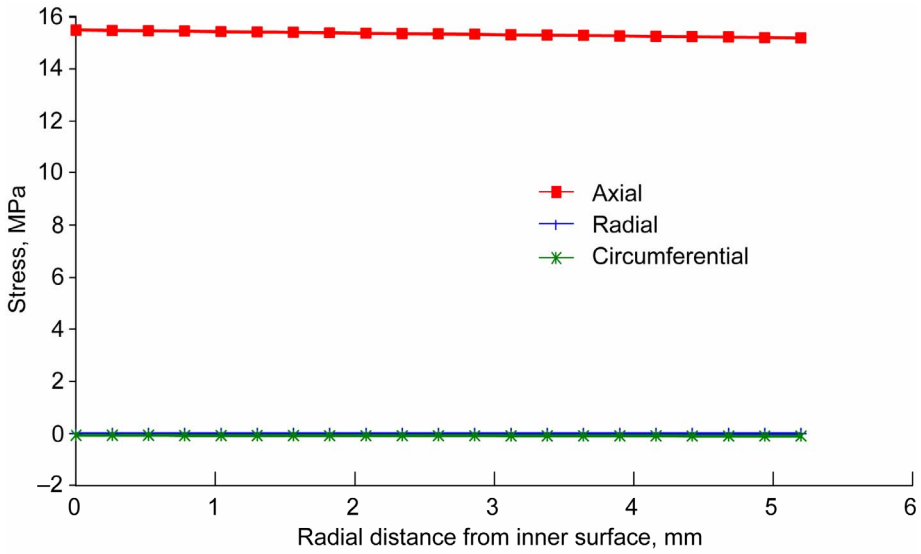

Figure 12.—Effect of axial force. Stress distribution on center section through wall thickness (radial direction).

3.2.4 Effect of axial force: center cross section

The maximum stress on the center plane of the specimen was in the axial direction. It was 15.49 MPa (2247 psi) at the inner surface and gradually reduced to 15.14 MPa (2196 psi) at the outer surface (see fig. 12). The other stress components maintained a value near zero through the wall thickness. Therefore, the stress distribution through the specimen wall at the center of the gauge section was relatively uniform although not perfectly uniform. This means that there was some small bending stress present.

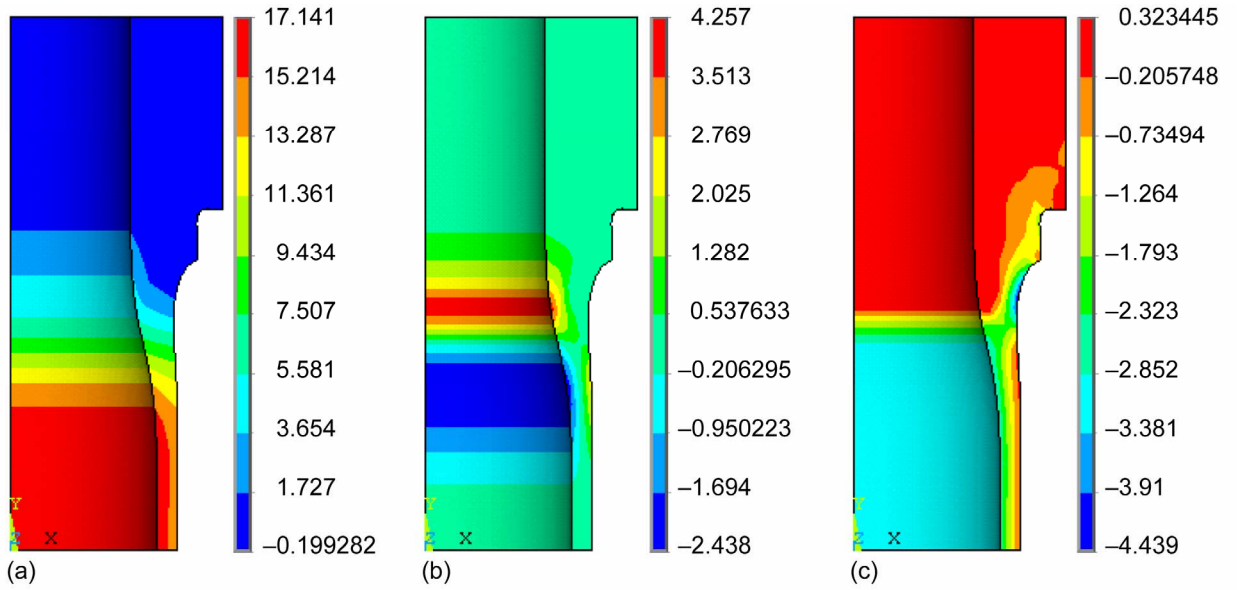

Figure 13.—Effect of internal pressure. (a) First principal stress. (b) Second principal stress. (c) Third principal stress.

3.3 Effect of Internal Pressure

3.3.1 ANSYS finite-element results: internal pressure

The ANSYS finite-element model was solved with a 2.84-MPa (412-psi) internal pressure applied on an area representing the middle 117.35 mm (4.62 in.) of the inside surface (shown in fig. 5(a)). Figure 13 shows the stress distributions.

3.3.2 Effect of internal pressure: inner surface

The effects of the 2.84-MPa (412-psi) pressure dominated the circumferential stress on the inner surface. The analysis showed that the peak circumferential stress was 17.04 MPa (2471 psi) at a location of 16.97 mm (0.67 in.) from the center. The stress at the center of the specimen was 16.92 MPa (2454 psi).

From table IV, it is seen that the stresses from the ANSYS analysis differed by less than 1 percent compared with the numerical result reported from ORNL.

TABLE IV.—COMPARISON OF NUMERICAL RESULTS: EFFECT OF INTERNAL PRESSURE ON INNER SURFACE

Finite-element analysis	Circumferential stress at center, MPa (psi)	Peak circumferential stress, MPa (psi)	Axial location[a] of peak stress, mm (in.)
ORNL	16.98 (2463)	17.06 (2474)	16.51 (0.65)
NASA	16.92 (2454)	17.04 (2471)	16.97 (0.67)
Difference, percent	0.4	0.1	[b]2.5

[a]Measured axially from center of specimen.
[b]Percentage difference relative to one-half gage length.

At the center of the specimen, the finite-element model had a stress that was 0.4 percent more than the Lamé stress equation that was calculated from (table V):

$$\sigma_\eta = \frac{P_i a^2}{b^2 - a^2}\left(1 + \frac{b^2}{r^2}\right) \tag{10}$$

where σ_η is the Lamé stress; P_i is the pressure on the inner surface; a is the inside radius; b is the outside radius; and r is the radius of interest.

TABLE V.—COMPARISON OF RESULTS AT INNER SURFACE: EFFECT OF INTERNAL PRESSURE

Results	Circumferential stress at center, MPa (psi)
Calculated Lamé stress	16.94 (2457)
NASA (finite-element analysis)	16.92 (2454)
Difference, percent	0.1

Figure 14 shows the ANSYS analysis results of the three stress components on the inner surface. This resulting graph exhibits a trend similar to that produced in the ORNL technical report (see the appendix). The axial stress, however, varied somewhat. The ORNL report showed a peak of 6.55 MPa (950 psi) at 64 mm (2.52 in.), whereas the ANSYS model had a peak of 4.83 MPa (701 psi) at a 64-mm (2.52-in.) distance from the center. The reason for the difference is unknown other than the previously mentioned difference in the mesh refinement and mandrel displacement, but relative to the CARES/Life analysis, the circumferential stress will dominate the probability of failure response such that the difference between the ORNL and NASA results is not an important issue.

3.3.3 Effect of internal pressure: outer surface

The maximum circumferential stress on the outer surface was 14.65 MPa (2125 psi). It occurred at the farthest point on the gauge section from the center. This stress was 3.1 percent larger than the FEA done by ORNL (see table VI). Note: the 14.2-MPa (2060-psi) value was read from the graph in the ORNL report.

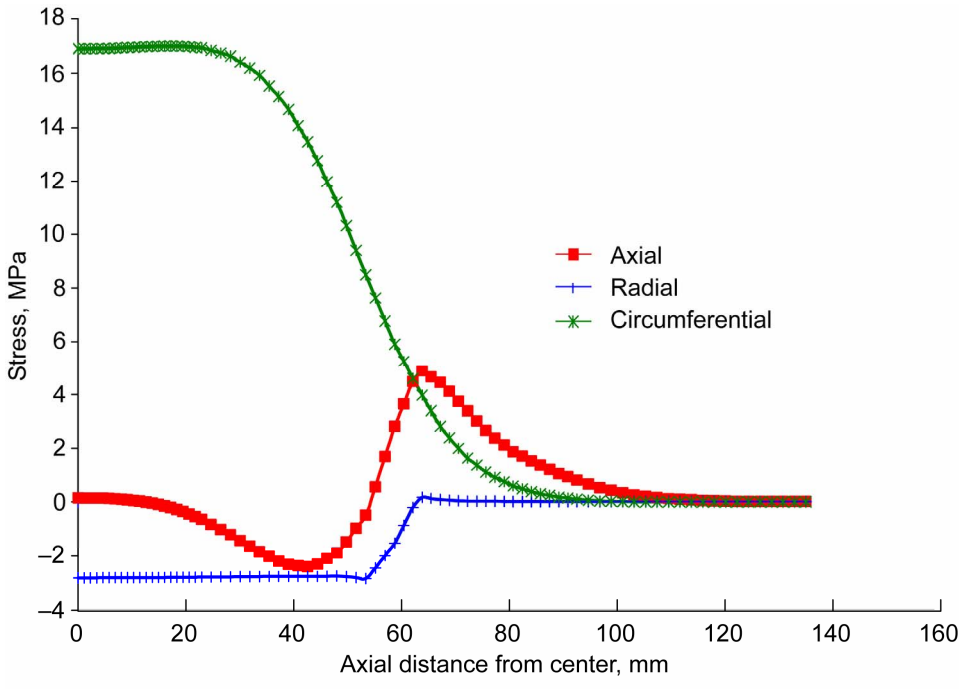

Figure 14.—Effect of internal pressure. Stress distribution on inner surface.

TABLE VI.—COMPARISON OF NUMERICAL RESULTS:
EFFECT OF INTERNAL PRESSURE ON OUTER SURFACE

Finite-element results	Peak circumferential stress, MPa (psi)
ORNL	14.20 (2060)
NASA	14.65 (2143)
Difference, percent	3.1

The ANSYS results were nearly identical to the calculated Lamé stress at the center (see table VII). Figure 15 shows a graph of the stresses along the gauge section. In general, the trend observed in the gauge section from the ORNL report was followed by the ANSYS model, indicating that the ANSYS model did not contain a significant and unexpected error. There was an increase in circumferential stress along the gauge length; the axial stress and radial stress components were negligible along the gauge length. Again, this indicated a slight stress concentration where the termination of the pressurized bladder and the beginning of the transition region occurred—which is undesirable.

TABLE VII.—COMPARISON OF CALCULATED RESULTS:
EFFECT OF INTERNAL PRESSURE

Results	Circumferential stress at center, MPa (psi)
Calculated Lamé stress	14.02 (2033)
NASA (finite-element analysis)	14.03 (2035)
Difference, percent	0.07

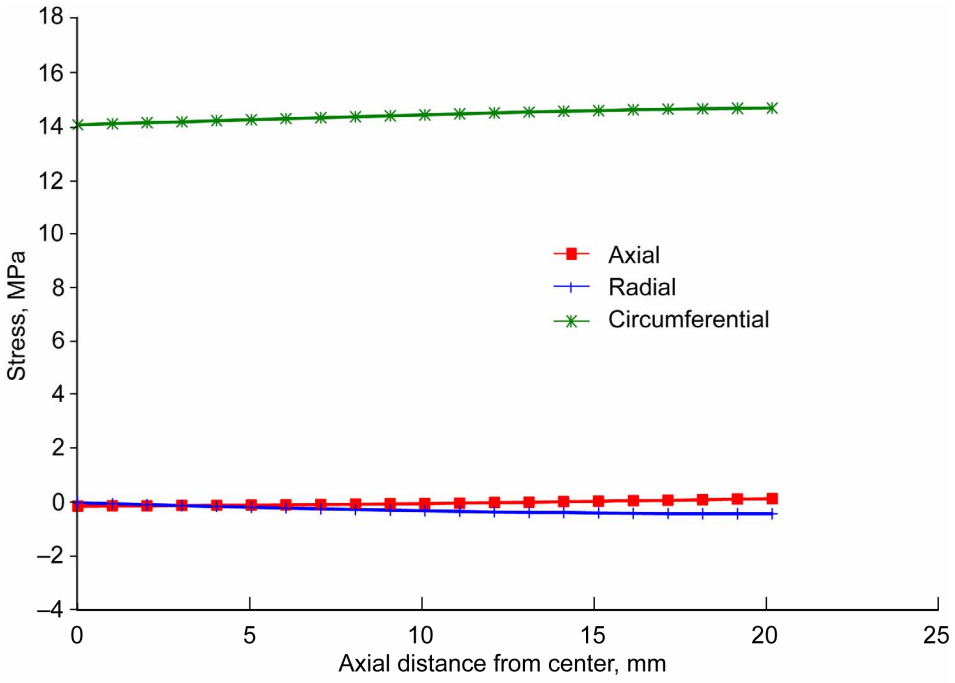

Figure 15.—Effect of internal pressure. Stress distribution on outer surface in gauge section of specimen.

3.3.4 Effect of internal pressure: center section

Figure 16 shows the stress distribution through the specimen wall at the center of the gauge section. Consistent with the Lamé stress, there is a stress gradient through the specimen wall for the circumferential stress. The radial stress is compressive on the inner wall and becomes zero on the outside wall as would be expected.

3.4 Effect of Combined Load

3.4.1 ANSYS finite-element results: combined load

The ANSYS finite-element model was solved with a 2.84-MPa (412-psi) internal pressure applied on an area representing the middle 117.4 mm (4.62 in.) of the inside surface and with an 11.01-MPa (1597-psi) pressure applied on the areas that represent the grips to simulate the 17.8-kN (4000-lb) axial load.

The finite-element model had the following stress distributions as shown in figure 17.

3.4.2 Effect of combined load: inner surface

When the model was loaded with the internal pressure and the axial force previously described in section 3.4.1, the maximum stress was circumferential. The maximum circumferential stress on the inner surface was 17.65 MPa (2560 psi) and occurred 26.4 mm (1.04 in.) from the center. The circumferential stress at the center was 16.86 MPa (2445 psi).

Compared with the FEA solution in the ORNL report, the circumferential stresses from the ANSYS model varied by less than 1 percent. The location of the peak stress, however, was farther along the gauge section (table VIII).

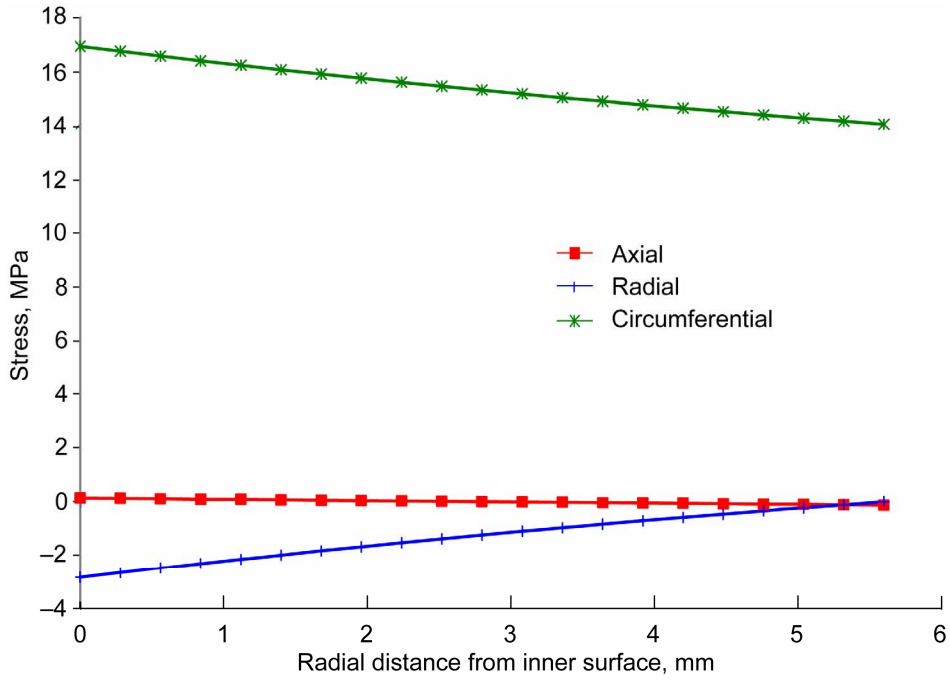

Figure 16.—Effect of internal pressure. Stress distribution on center plane through specimen wall (radial direction).

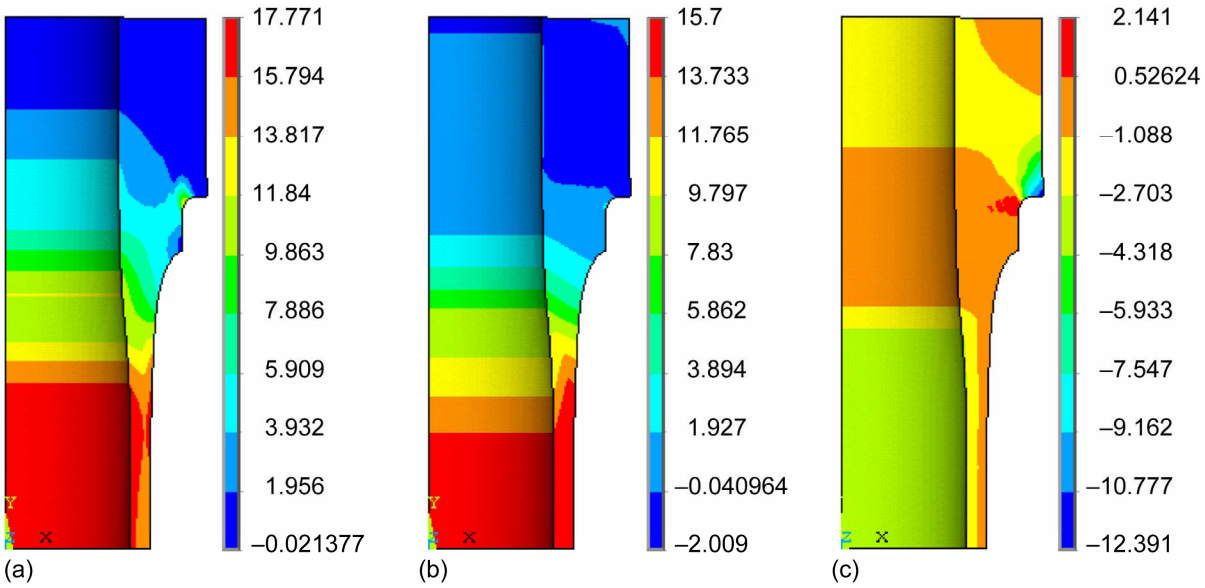

Figure 17.—Effect of combined axial and pressure loads. (a) First principal stress. (b) Second principal stress. (c) Third principal stress.

TABLE VIII.—COMPARISON OF NUMERICAL RESULTS: EFFECT OF BOTH LOADS ON INNER SURFACE

Finite-element analysis	Circumferential stress at center, MPa (psi)	Peak circumferential stress, MPa (psi)	Axial location[a] of peak stress, mm (in.)
ORNL	16.95 (2458)	17.53 (2542)	22.86 (0.90)
NASA	16.86 (2445)	17.65 (2560)	26.43 (1.04)
Difference, percent	0.5	0.7	[b]16

[a]Measured from center of specimen.
[b]Percentage difference relative to one-half gage length.

The calculated Lamé stress was 16.86 MPa (2445 psi). The stress from the ANSYS model matched this value at the center of the specimen. The axial stress from the ANSYS model was 15.62 MPa (2265 psi) whereas from the ORNL ADINA model, it was estimated to be 15.9 MPa (2306 psi) for an approximately 2-percent difference. Figure 18 shows the stress distributions along the inner surface measured from the centerline. The graph follows the general trend of the ORNL results, although the circumferential stress deviated somewhat after 100 mm (3.94 in.), and the local peak of the axial stress was 64 mm (2.52 in.) in the ANSYS model rather than 66 mm (2.60 in.) as reported by ORNL (see also the appendix). These differences were likely due to the ANSYS model's not having the enforced displacement of the mandrel.

3.4.3 Effect of combined load: outer surface

The maximum axial stress on the outer surface was 15.84 MPa (2297 psi) and occurred at the end of the gauge section. The peak circumferential stress was 14.97 MPa (2171 psi), also at the end of the gauge section. These results compared with the 16.3-MPa (2364-psi) axial stress and the 14.8-MPa (2147-psi) circumferential stress at the end of the gauge section from the ORNL analysis (estimated from graph) for a difference of 2.8 and 1.1 percent, respectively.

At the center (along the axial length) of the specimen, the axial stress results from the ANSYS analysis were less than 1 percent larger than the FEA done by ORNL (table IX). The ORNL result was estimated from their graph.

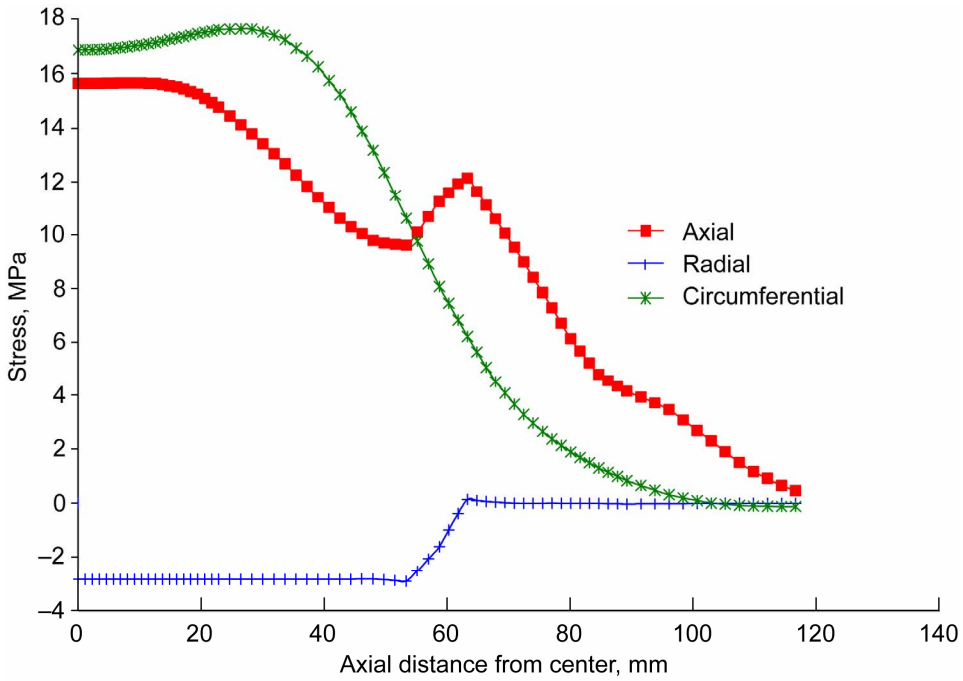

Figure 18.—Effect of combined loads. Stress distribution on inner surface measured from centerline.

TABLE IX.—COMPARISON OF NUMERICAL RESULTS: EFFECT OF BOTH LOADS

Finite-element analysis results	Axial stress at center, MPa (psi)
ORNL	14.90 (2161)
NASA	15.03 (2180)
Difference, percent	0.9

For the circumferential stress at the center of the specimen, the ANSYS analysis was 1 percent larger than the ORNL ADINA FEA (table X), which was within the measurement margin of error. Note: the 15.3-MPa (2219-psi) value was estimated from figure 12 in the ORNL report.

TABLE X.—COMPARISON OF NUMERICAL RESULTS: EFFECT OF BOTH LOADS

Finite-element analysis results	Circumferential stress at center, MPa (psi)
ORNL	13.80 (2002)
NASA	13.94 (2022)
Difference, percent	1.0

Figure 19 shows a plot of the ANSYS FEA stresses along the outer surface of the gauge section. The ANSYS model follows the trend shown in the graph from the ORNL report. In the gauge section, the axial stress starts at about 15 MPa (2176 psi) at the center and increases about 1 MPa (145 psi) towards the end of the gauge section. The circumferential stress follows a similar pattern.

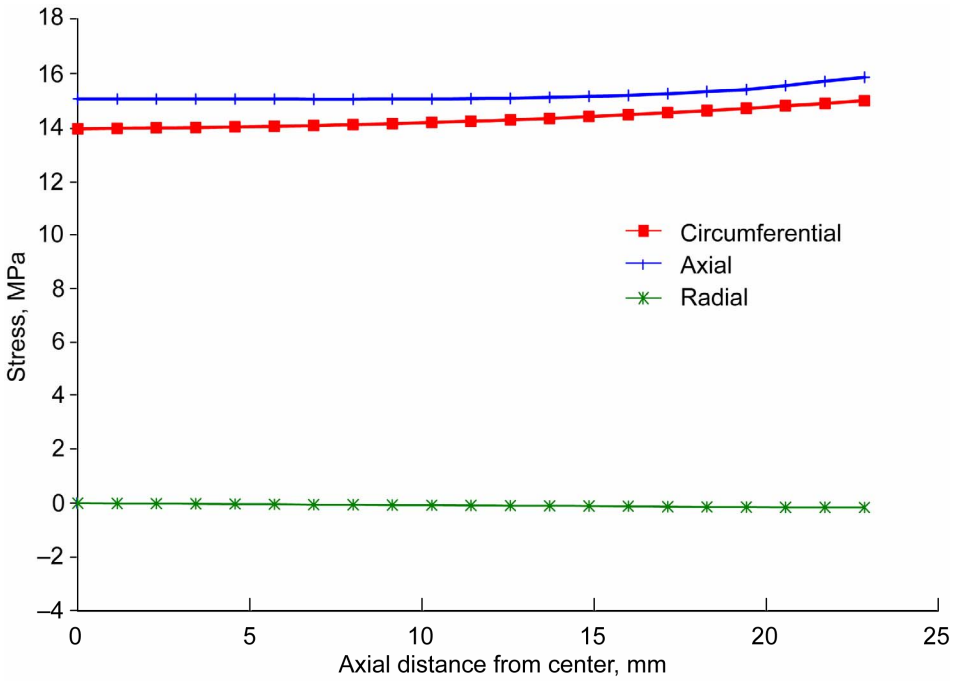

Figure 19.—Effect of combined loads. Stress distribution on outer surface measured from centerline.

3.4.4 Effect of combined load: center section

The maximum stress on the center plane of the specimen is in the circumferential direction. It is 16.86 MPa (2445 psi) and occurs at the inner surface. The peak axial stress is 15.62 MPa (2265 psi), also at the inner surface. Figure 20 shows a plot of the stresses at the center through the specimen wall.

3.5 Summary of ANSYS Results

The results from the ANSYS analysis generally followed the ADINA analysis results from the ORNL technical report for the different load cases. This provided additional confidence that the ANSYS results could be used to perform the CARES/Life analysis. The magnitude of peak stresses was reasonably consistent, although the location of the peak stresses varied somewhat. This variance may be due to not applying the displacement of the mandrel as was done in the ORNL analysis. Also, the higher mesh density, in addition to using different versions of different FEA codes, could also have made a difference. The ADINA model developed by the ORNL researchers was validated within 7.8 percent against strain gauge testing on an aluminum specimen with the gauges located on the specimen outside gauge surface. Therefore, since the ANSYS model generated for this effort matched the ADINA model reasonably well, the ANSYS model was judged to be suitable to perform the CARES/Life reliability analysis for multiaxial stress states and to be able to accurately compare with the experimentally generated failure data by ORNL. The stress reanalysis performed herein also brought attention to the significant stress concentration at the fillet adjacent to the grip and to the mild stress concentration that occurred at the end of the gauge section. These are undesirable because stress concentrations occurring outside the gauge section can be sites of failure that compete with failure initiating inside the gauge section—and failure always occurring within the gauge section is needed in order that the experimental results be valid. Unfortunately, it is difficult to design the specimen without some stress concentrations, but it is important to minimize them as much as possible.

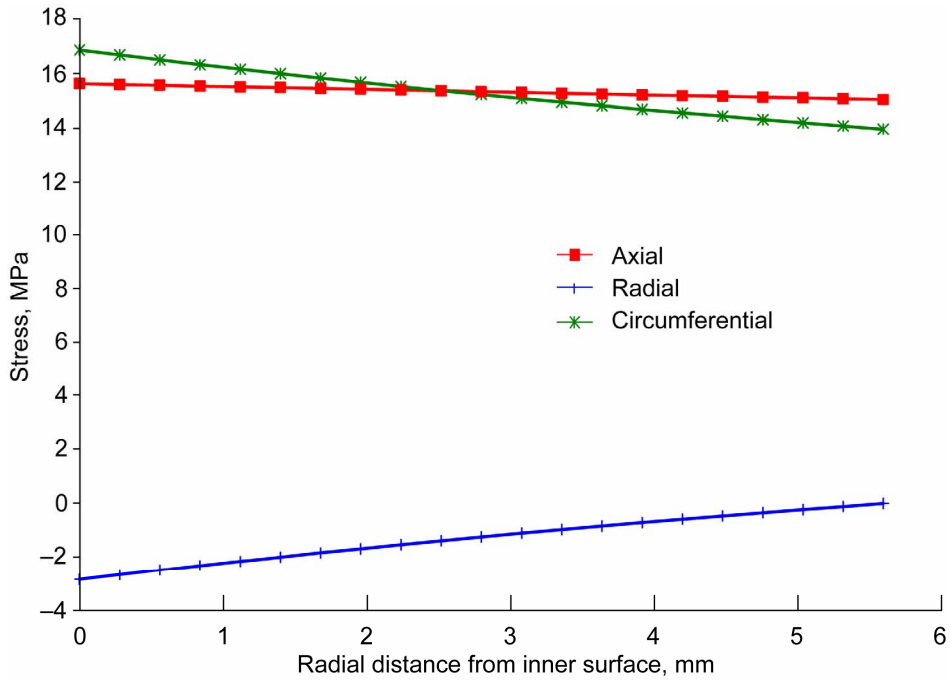

Figure 20.—Effect of combined loads. Stress distribution on center plane through wall (radial direction).

3.6 Generating Graphite Specimen Failure Envelopes

Creating the failure envelopes involved using ANSYS and CARES together. To create the biaxial stress state, two loads were applied: an axial force and a pressure on the internal surface. By adjusting these loads in ANSYS, the magnitude of the stresses and the degree of mulitaxiality of the stress state were varied. The results from the FEA were input to CARES to calculate the failure probability of the loaded specimen. The principal stresses on the outer surface of the specimen at the center of the specimen were used to determine the multiaxial stress state. The resulting data were plotted to generate the failure envelope. This was consistent with the ORNL report, which used strain gauges on the outer surface at the center of the specimen (see fig. 6) to obtain the strains (and hence the stresses) at the instant of failure.

The failure envelopes were created using three failure criteria: PIA, Batdorf, and Weibull normal stress averaging. The Batdorf criterion was used twice for values of $\overline{C}$ of 0.82 and 1.20. These values were chosen to show a case of high shear sensitivity and a case that best fit the data, respectively. The PIA criterion was tested using principal stresses.

The Weibull parameters used are shown in table XI. It should be noted that the parameters were computed using the experimental data from the ORNL multiaxial specimen for the axial loading case using the maximum likelihood method. Volume flaws were assumed for the analysis. The value of the scale parameter σ_{oV} was calibrated using CARES along with the finite-element model of the specimen for the case of axial loading, whereby the level of loading yielded the value of the characteristic strength σ_θ as the first principal stress on the outer surface of the specimen at the centerline. The value of σ_{oV} was then adjusted so that a predicted probability of failure of 63.21 percent was obtained for that particular level of axial loading.

TABLE XI.—WEIBULL PARAMETERS USED FOR RELIABILITY ANALYSIS

Scale parameter, σ_{oV}, MPa · mm$^{1/22.43}$ (psi · in.$^{1/22.43}$)	42.69 (4017)
Weibull modulus, m_V	22.43
Characteristic strength, σ_θ , Mpa (psi)	26.38 (3826)

The resulting failure envelopes are shown in figures 21 through 24. The failure envelopes were generated for predicted probabilities of failure of 10, 50, and 90 percent. All criteria matched the experimental data in the tension-tension quadrant reasonably well. There was some deviation between prediction and experimental results for pure pressure loading (only hoop stress and no axial stress). This deviation was due to the IG–110 material being slightly anisotropic. No attempt was made to consider anisotropy in the multiaxial failure theories used herein. For design purposes, the conservative practice would be to normalize the multiaxial failure envelopes to the uniaxial strength in the weakest material direction; in this case, that would be in the hoop stress or *x*,*z*-plane as defined in figure 7(a). In the tension-compression quadrant, the Batdorf criterion followed the experimental data closest. Figure 23 shows the results for $\overline{C}$ = 0.82. Figure 24 shows the results for $\overline{C}$ = 1.20, a value chosen to improve the fit to the data. Figure 24 showed quite good correlation to the data. The $\overline{C}$ of 1.2 indicated a fairly high shear sensitivity for the material. The results observed in this report—that a Batdorf style multiaxial model correlated best to experimental data—are consistent with the results reported by Uchimura, Kokaji, and Kaji (1992) on silicon nitride material.

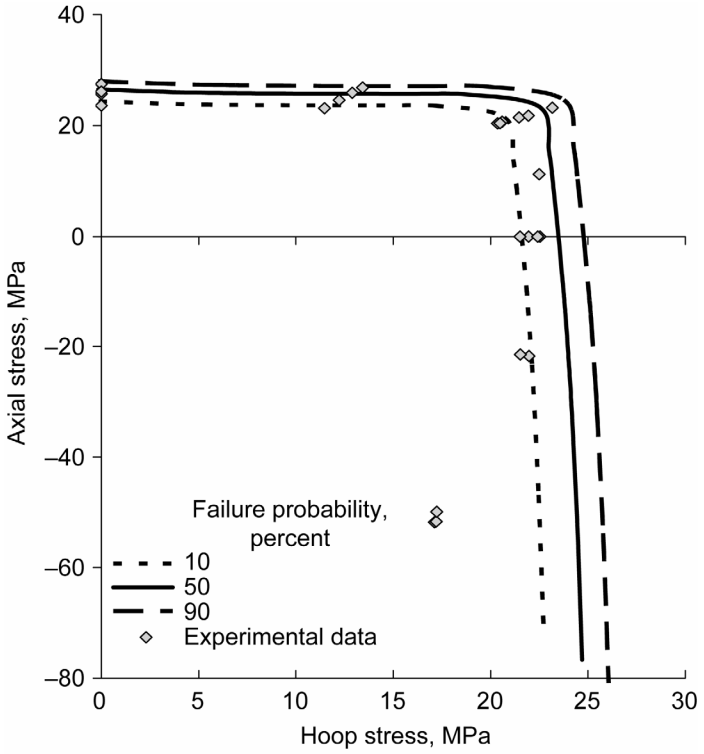

Figure 21.—Failure envelope based on principle of independent action (PIA).

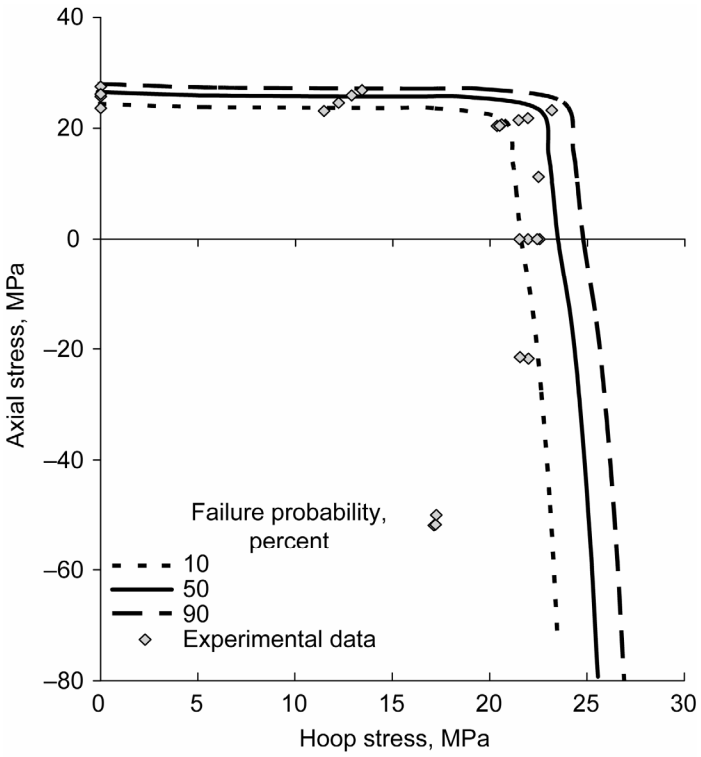

Figure 22.—Failure envelope based on Weibull normal stress averaging.

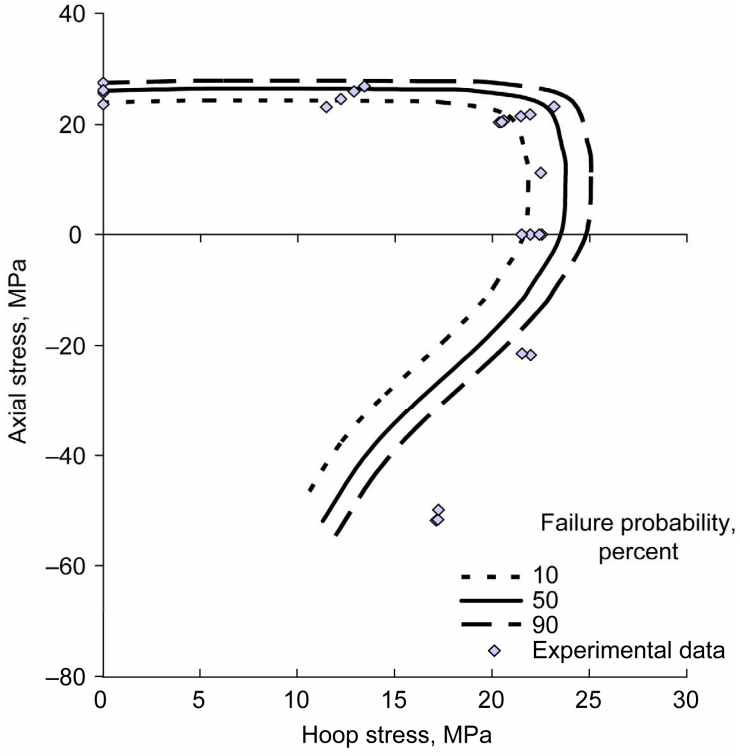

Figure 23.—Failure envelope based on Batdorf multiaxial failure theory for $\bar{C}$ = 0.82.

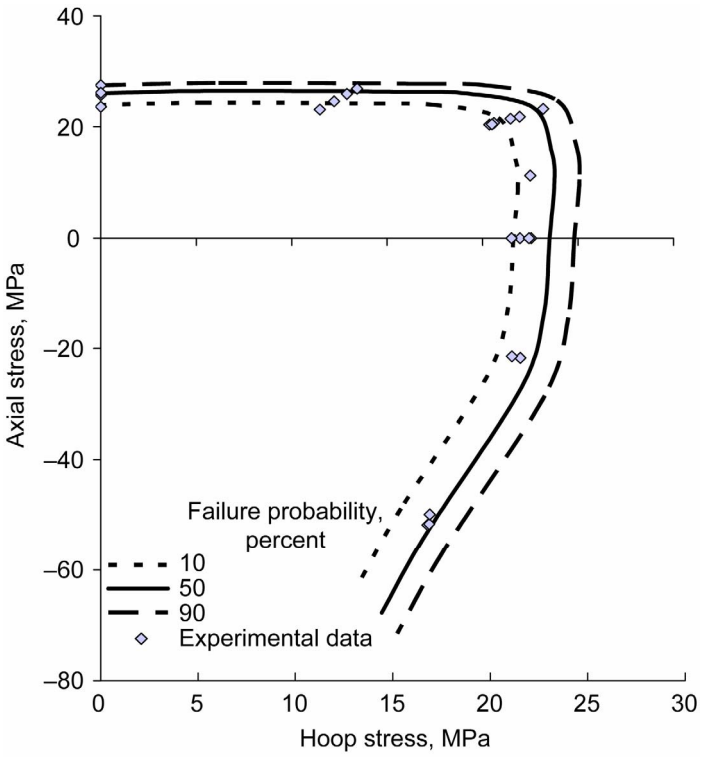

Figure 24.—Failure envelope based on Batdorf multiaxial failure theory for $\bar{C}$ = 1.20.

4. Conclusion

An ANSYS finite-element model of the Oak Ridge National Laboratory (ORNL) multiaxial specimen for IG–110-grade graphite material was developed and satisfactorily verified for multiaxial loading using various combinations of axial and internal pressure loading. The fillet near the grip bearing area for axial tensile load had a significant stress concentration that, although lower than the stress in the gauge region, was still sufficiently high to be of potential concern as a possible site where specimen failure could occur. A slight stress concentration at the transition from the gauge section was also noted. Using the results from finite-element analysis (FEA) with CARES/Life (The Ceramics Analysis and Reliability Evaluation of Structures Life prediction code) enabled the prediction of the probability of failure of the specimen geometry for various combinations of axial and pressure loading. Using CARES/Life, the principle of independent action (PIA), Weibull normal stress averaging, and Batdorf multiaxial failure theories were compared. The results from this study showed that the Batdorf theory correlated best to the experimental data and therefore should used to predict the reliability of isotropic grade graphite structures under generalized multiaxial loading. The Batdorf analysis procedure (at least to account for multiaxial stress states) should be included in design standards, such as the ASME Boiler and Pressure Vessel Code for graphite structures to be used in nuclear power plants.

Appendix—Comparison of Finite-Element Analysis (FEA) Results on Inside Surface of Specimen

The forthcoming figures compare results of the NASA FEA with the analysis performed by ORNL for the inside surface of the specimen. The results are compared in English units, which is consistent with the original figures in the ORNL report.

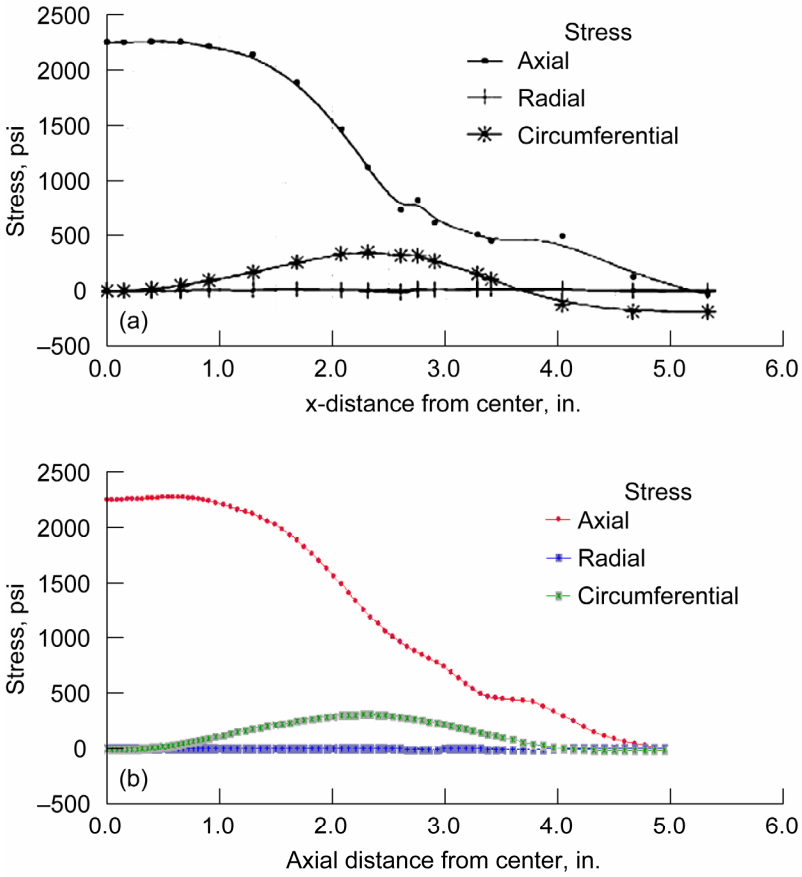

Figure 25.—Stress along inner surface from 4000-lb axial load. (a) ORNL results reproduced from Hobson, D.O. (1994) and Yahr, et al. (1993) (Multiaxial Tests of H–451 Graphite. ORNL/NPR–93/13, vol. 1, 1993, not published. Available from Carbon Materials Technology Group, ORNL.). (b) NASA results.

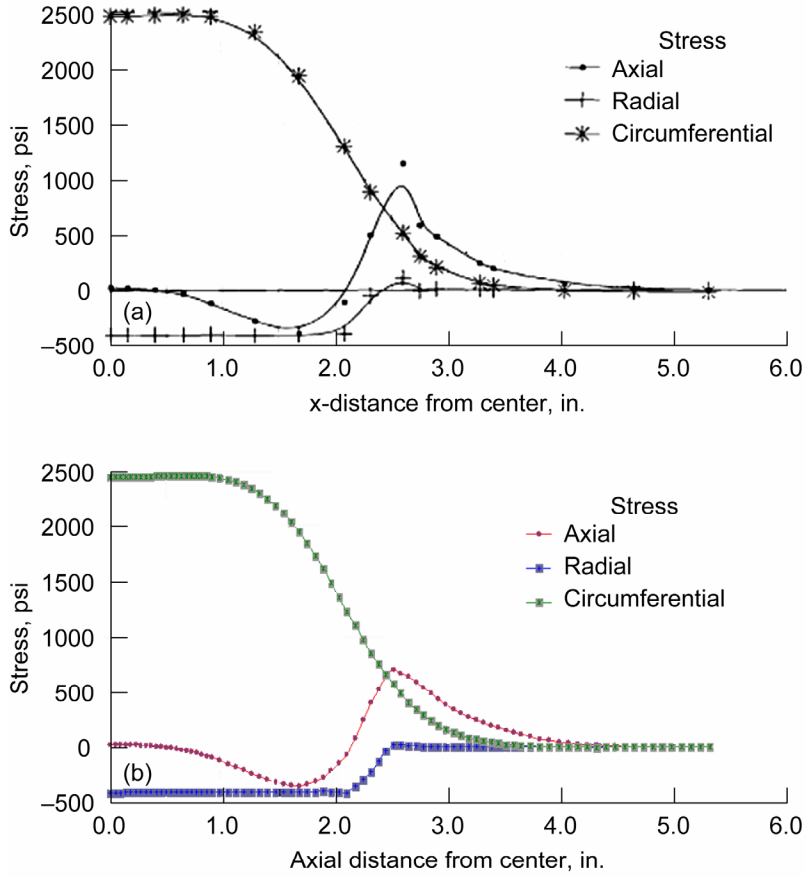

Figure 26.—Stress along inner surface from 412-psi internal pressure load. (a) ORNL results reproduced from Hobson, D.O. (1994) and Yahr, et al. (1993) (Multiaxial Tests of H–451 Graphite. ORNL/NPR–93/13, vol. 1, 1993, not published. Available from Carbon Materials Technology Group, ORNL.). (b) NASA results.

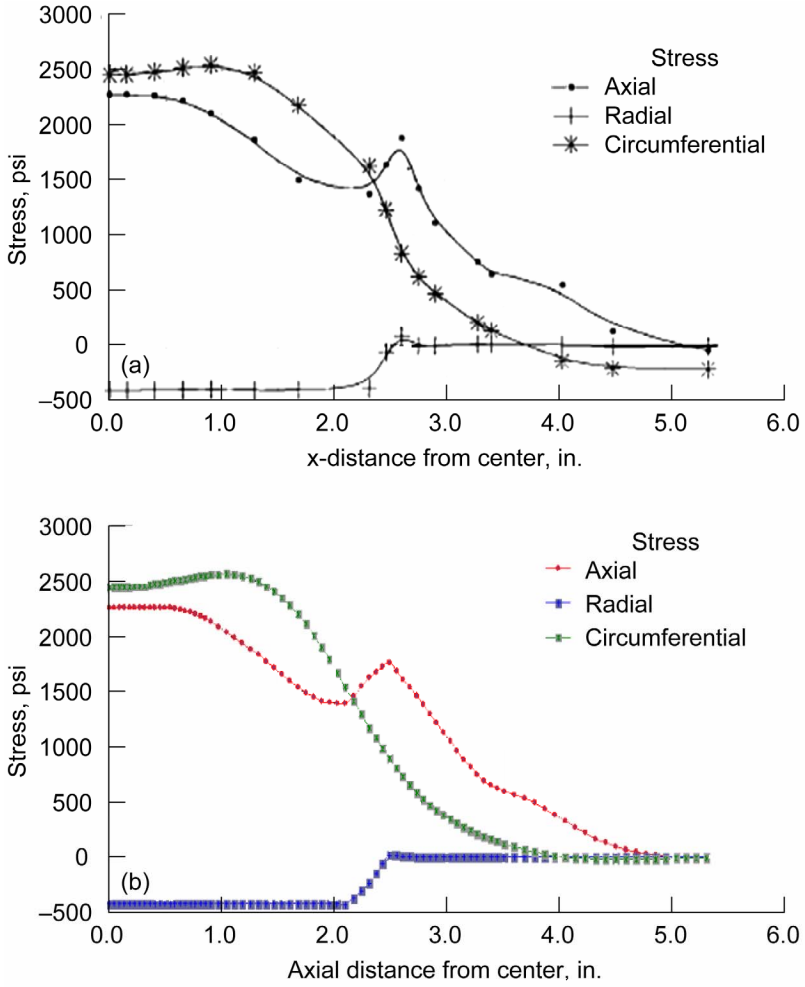

Figure 27.—Stress along inner surface from 4000-lb axial load and 412-psi internal pressure load. (a) ORNL results reproduced from Hobson, D.O. (1994) and Yahr, et al. (1993) (Multiaxial Tests of H–451 Graphite. ORNL/NPR–93/13, vol. 1, not published. Available from Carbon Materials Technology Group, ORNL.). (b) NASA results.

References

A Technology Roadmap for Generation IV Nuclear Energy Systems. U.S. D.O.E. Nuclear Energy Research Advisory Committee and the Generation IV International Forum, GIF−002−00, 2002. http://gif.inel.gov/roadmap/ Accessed June 13, 2008.

Barnett, R.L., et al.: Fracture of Brittle Materials Under Transient Mechanical and Thermal Loading. AFFDL−TR−66−220, 1967.

Batdorf, S.B.; and Crose, J.G.: Statistical Theory for the Fracture of Brittle Structures Subjected to Nonuniform Polyaxial Stresses. J. App. Mech., vol. 41, series E, no. 2, 1974, pp. 459−464.

Batdorf, S.B.; and Heinisch, H.L., Jr.: Weakest Link Theory Reformulated for Arbitrary Fracture Criterion. J. Am. Ceram. Soc., vol. 61, nos. 7−8, 1978, pp. 355−358.

Eto, Motokuni, et al.: The Biaxial Strength and Fracture Criteria for HTGR Graphites. JAEA-Research/JAERI-Research 96−016, 1996.

Freudenthal, Alfred M.: Statistical Approach to Brittle Fracture. Fracture, H. Liebowitz, ed., Vol. II, ch. 6, Academic Press, New York, NY, 1968, pp. 591−619.

Grade IG−11: Toyo Tanso USA, Inc., Troutdale, OR, 2006. http://www.ttu.com/Grade_IG-11.html Accessed June 18, 2008.

Hobson, D.O. MHTGR Program Annual Report for January 1, 1989, Through June 30, 1993. DOE−HTGR−90−389, Rev. 0, ORNL−6779, 1994.

Holt, M.J.: Issues of Scale and the Functionality of Polygranular Graphite Components. The University of Hull, United Kingdom. http://www.eng.hull.ac.uk/research/Graphite/index.htm Accessed June 18, 2008.

MacDonald, P.E.: Next Generation Nuclear Plant Research and Development Program Plan. INEEL/EXT−05−02581, 2005. http://www.inl.gov/technicalpublications/Documents/3028298.pdf Accessed June 18, 2008.

Nemeth, Noel N., et al.: Designing Ceramic Components for Durability. Am. Cer. Soc. Bul., vol. 72, no. 12, 1993, pp. 59−69.

Nemeth, Noel, N., et al.: CARES/Life Ceramics Analysis and Reliability Evaluation of Structures Life Prediction Program. NASA/TM—2003-106316, 2003.

Nemeth, Noel N.; Gyekenyesi, John, P.; and Jadaan, Osama M.: Lifetime Reliability Prediction of Ceramic Structures Under Transient Thermomechanical Loads. NASA/TP—2005-212505, 2005.

Rittenhouse, P.L.: GT−MHR Annual Progress Report for Period June 1993 Through June 1994. ORNL−6850 (DOE−HTGR−100−242), 1995.

Uchimura, H.; Kokaji, A.; and Kaji, M.: Evaluation of Fast Fracture Strength of Ceramic Components Under Multiaxial Stress States. IGTI ASME Turbo Expo '92 Paper No. 92−GT−384, 1992.

Weibull, W.: Phenomenon of Rupture in Solids. Ingenoirsvetenskapsakad. Handl., no. 153, 1939.

Weibull, Waloddi: A Statistical Distribution of Wide Applicability. J. App. Mech., vol. 18, 1951, pp. 293−297.

Yahr, et al.: Multiaxial Tests of H−451 Graphite. ORNL/NPR−93/13, vol. 1, 1993. Available from Carbon Materials Technology Group, Oak Ridge National Laboratory.

REPORT DOCUMENTATION PAGE	Form Approved OMB No. 0704-0188

1. REPORT DATE *(DD-MM-YYYY)*	2. REPORT TYPE	3. DATES COVERED *(From - To)*
01-08-2008	Technical Memorandum	

4. TITLE AND SUBTITLE
Reliability Assessment of Graphite Specimens Under Multiaxial Stresses

5a. CONTRACT NUMBER

5b. GRANT NUMBER

5c. PROGRAM ELEMENT NUMBER

6. AUTHOR(S)
Sookdeo, Steven; Nemeth, Noel, N.; Bratton, Robert, L.

5d. PROJECT NUMBER

5e. TASK NUMBER

5f. WORK UNIT NUMBER
WBS 984754.02.07.03.16.03

7. PERFORMING ORGANIZATION NAME(S) AND ADDRESS(ES)
National Aeronautics and Space Administration
John H. Glenn Research Center at Lewis Field
Cleveland, Ohio 44135-3191

8. PERFORMING ORGANIZATION REPORT NUMBER
E-16475

9. SPONSORING/MONITORING AGENCY NAME(S) AND ADDRESS(ES)
National Aeronautics and Space Administration
Washington, DC 20546-0001

10. SPONSORING/MONITORS ACRONYM(S)
NASA

11. SPONSORING/MONITORING REPORT NUMBER
NASA/TM-2008-215204

12. DISTRIBUTION/AVAILABILITY STATEMENT
Unclassified-Unlimited
Subject Category: 39
Available electronically at http://gltrs.grc.nasa.gov
This publication is available from the NASA Center for AeroSpace Information, 301-621-0390

13. SUPPLEMENTARY NOTES

14. ABSTRACT
An investigation was conducted to predict the failure strength response of IG-100 nuclear grade graphite exposed to multiaxial stresses. As part of this effort, a review of failure criteria accounting for the stochastic strength response is provided. The experimental work was performed in the early 1990s at the Oak Ridge National Laboratory (ORNL) on hollow graphite tubes under the action of axial tensile loading and internal pressurization. As part of the investigation, finite-element analysis (FEA) was performed and compared with results of FEA from the original ORNL report. The new analysis generally compared well with the original analysis, although some discrepancies in the location of peak stresses was noted. The Ceramics Analysis and Reliability Evaluation of Structures Life prediction code (CARES/Life) was used with the FEA results to predict the quadrants I (tensile-tensile) and quadrant IV (compression-tension) strength response of the graphite tubes for the principle of independent action (PIA), the Weibull normal stress averaging (NSA), and the Batdorf multiaxial failure theories. The CARES/Life reliability analysis showed that all three failure theories gave similar results in quadrant I but that in quadrant IV, the PIA and Weibull normal stress-averaging theories were not conservative, whereas the Batdorf theory was able to correlate well with experimental results. The conclusion of the study was that the Batdorf theory should generally be used to predict the reliability response of graphite and brittle materials in multiaxial loading situations.

15. SUBJECT TERMS
Multiaxial; Graphite; Weibull; Reliability; Fracture; Batdorf; CARES/Life; Nuclear; Failure; Probability

16. SECURITY CLASSIFICATION OF:			17. LIMITATION OF ABSTRACT	18. NUMBER OF PAGES	19a. NAME OF RESPONSIBLE PERSON
a. REPORT	b. ABSTRACT	c. THIS PAGE			STI Help Desk (email:help@sti.nasa.gov)
U	U	U	UU	37	19b. TELEPHONE NUMBER *(include area code)* 301-621-0390